JOURNAL OF PROPULSION AND POWER
Vol. 18, No. 4, July–August 2002

# Thermomechanical Analysis and Optimization of Cryogenic Liquid Rocket Engines

Detlef Kuhl*
*Ruhr-University Bochum, D-44780 Bochum, Germany*
and
Jörg Riccius† and Oskar J. Haidn‡
*DLR, German Aerospace Research Center, D-74239 Hardthausen, Germany*

**A coupled finite element fluid–structure interaction analysis of regeneratively cooled rocket combustion chambers, which allows the computation of the coolant flow and the heat conduction between the coolant and the combustion chamber structure, is presented. Furthermore, the resulting elasto–plastic deformation of the combustion chamber under cyclic thermal and mechanical loading is analyzed. The developed solution strategy is applied to the prediction of the heat transfer and thermomechanical load-induced deformation process of the European rocket engine Vulcain. Based on the results, the failure mechanism of the combustion chamber and its governing parameters are identified. It is demonstrated that this mechanism significantly reduces the lifetime of the rocket engine. Besides the conceptual design by the engineer, a mathematical optimization procedure based on the finite element model of the combustion chamber is investigated. This optimization method allows the improvement of an initial design with respect to a finite number of design variables such that the stress, plastic strain, or temperature levels are decreased, and accordingly, the lifetime will be increased.**

## Nomenclature

| | | |
|---|---|---|
| $A$ | = | cooling channel cross section, m$^2$ |
| $\boldsymbol{B}_n$ | = | approximated inverse Hessian |
| $c$ | = | specific heat, J/kgK |
| $E$ | = | Young's modulus, Pa |
| $e$ | = | internal energy, m$^2$/s$^2$ |
| $e_t$ | = | total energy, m$^2$/s$^2$ |
| $f$ | = | objective function |
| $\boldsymbol{g}$ | = | constraint vector |
| $g_i$ | = | single constraint |
| $H$ | = | hardening modulus, Pa |
| $h$ | = | cooling channel high, m |
| $\boldsymbol{I}_2$ | = | second-order identity tensor |
| $\boldsymbol{I}_4$ | = | fourth-order identity tensor |
| $i, j$ | = | arbitrary indices |
| $\boldsymbol{m}$ | = | normal vector yield surface |
| $\boldsymbol{n}$ | = | unit normal vector |
| $P$ | = | penalty function |
| $p$ | = | pressure, Pa |
| $p_p$ | = | penalty factor |
| $Q$ | = | constraint objective function |
| $\boldsymbol{q}$ | = | heat flux vector, W/m$^2$ |
| $q_i$ | = | normal heat flux, W/m$^2$ |
| $r_i$ | = | inner chamber radius, m |
| $r_e$ | = | outer chamber radius, m |
| $\boldsymbol{S}_n$ | = | search direction |
| $\boldsymbol{s}$ | = | vector of design variables |
| $s_i$ | = | single design variable |
| $T$ | = | tangent modulus, Pa |
| $t$ | = | chamber wall thickness, m |
| $t_c$ | = | coating thickness, m |
| $\boldsymbol{u}$ | = | displacement vector, m |
| $\dot{\boldsymbol{u}}$ | = | velocity vector, m/s |
| $x, y, z$ | = | coordinates |
| $\boldsymbol{x}$ | = | position vector, m |
| $\alpha$ | = | thermal expansion coefficient, 1/K |
| $\boldsymbol{\alpha}$ | = | tensor of hardening variables, Pa |
| $\alpha_i$ | = | film coefficient, W/m$^2$K |
| $\alpha_n$ | = | step length |
| $\beta$ | = | design segment angle, deg |
| $\Gamma_i$ | = | boundary |
| $\gamma$ | = | cooling channel angle, deg |
| $\Delta$ | = | difference |
| $\boldsymbol{\varepsilon}$ | = | strain tensor |
| $\theta$ | = | total temperature, K |
| $\theta_i$ | = | bulk temperature, K |
| $\theta_r$ | = | reference temperature, K |
| $\Lambda$ | = | conductivity, W/mK |
| $\lambda$ | = | load factor |
| $\mu$ | = | dynamic viscosity, Pa/s |
| $\nu$ | = | Poisson ratio |
| $\rho$ | = | density, kg/m$^3$ |
| $\boldsymbol{\sigma}$ | = | stress tensor, Pa |
| $\sigma_v$ | = | von Mises equivalent stress, Pa |
| $\sigma_Y$ | = | yield stress, Pa |
| $\boldsymbol{\tau}$ | = | viscous shear tensor, Pa |
| $\Omega_i$ | = | domain |
| $\nabla$ | = | gradient with respect to $\boldsymbol{x}$ |
| $\nabla_s$ | = | derivative with respect to $\boldsymbol{s}$ |
| $\nabla^{\text{sym}}$ | = | symmetric part of the gradient |
| $\nabla\cdot$ | = | divergence with respect to $\boldsymbol{x}$ |

*Subscripts*

| | | |
|---|---|---|
| $c$ | = | cooling channel |
| $cs$ | = | symmetry (cooling channel) |
| cu | = | copper |
| eff | = | effective value |
| global | = | global value |
| $h$ | = | hot-gas side |
| local | = | local value |

Received 22 September 2000; revision received 1 October 2001; accepted for publication 15 October 2001. 

*Oberingenieur, Institute for Structural Mechanics.
†Head, Theoretical Modeling Group, Institute of Space Propulsion. Member AIAA.
‡Head, Technology Department, Institute of Space Propulsion. Senior Member AIAA.

max = maximal value
min = minimal value
$n$ = iteration counter
ni = nickel
$s$ = structure
$ss$ = symmetry (structure)
$t$ = turbulent
0 = initial
1 = inlet
2 = outlet
$*$ = initial design
$\_$ = lower bound

*Superscripts*

$e$ = elastic
ep = elasto–plastic
$p$ = plastic
$\theta$ = thermal
$-$ = upper bound
$\cdot$ = time derivative

## I. Introduction

THE cryogenic hydrogen/oxygen-powered Vulcain engine is the main stage of the European Ariane 5 space transportation system. Figure 1 shows the scheme of this regeneratively cooled gas generator cycle engine. At the nominal operating point of 11 MPa, the peak heat load in the throat area exceeds 80 MW/m$^2$. The regenerative cooling introduces an enormous temperature gradient across the combustion chamber walls yielding large heat flux and thermal strains. The resulting plastic deformations of the wall material limit the combustion chamber lifetime. Experimental investigations by Quentmeyer[1,2] have demonstrated that low-cycle fatigue and creep are the main reasons for material failure. Figure 2 shows a combustion chamber cross section emphasizing characteristic features of a regeneratively cooled combustion chamber such as cooling channel geometry, failure location, chamber wall, and outer liner materials.

### A. Motivation

The increasing requirements regarding the performance of cryogenic liquid rocket engines in combination with the need to reduce continuously the operational cost has led to the idea of reusable space transportation systems. Because all reusable systems are based on an increased combustion chamber life time, the current research and technology activities at DLR, German Aerospace Research Center, Lampoldshausen aim at:

1) a detailed understanding of the failure mechanisms,
2) the development of a tool for the prediction of the combustion chamber life, and
3) an optimized design of the combustion chamber.

Before these items can be realized, the general problem of heat and mass transfer in a combustion chamber of a liquid rocket engine has to be solved: the prediction of injection, atomization, mixing, and combustion of the propellant, as well as the hot-gas flow in the combustion chamber, the heat transfer from the hot-gas side to the wall, further into the structure, and into the coolant, and, finally, the coolant flow itself. The basis for a deeper understanding of the failure mechanisms of current combustion chamber designs are detailed experimental data, material, and failure laws, as well as numerical simulations of the structural behavior (see Kuhl et al.[3] and Kuhl[4]). The automatic design optimization requires the solution of the inverse thermomechanical problem. Therefore, optimization methods will be applied to improve future developments of combustion chambers.[5] It is expected that the combination of the design tools and results yields an improvement of both coolant-side heat transfer and the combustion chamber geometry and will increase the lifetime of cryogenic liquid rocket engines.

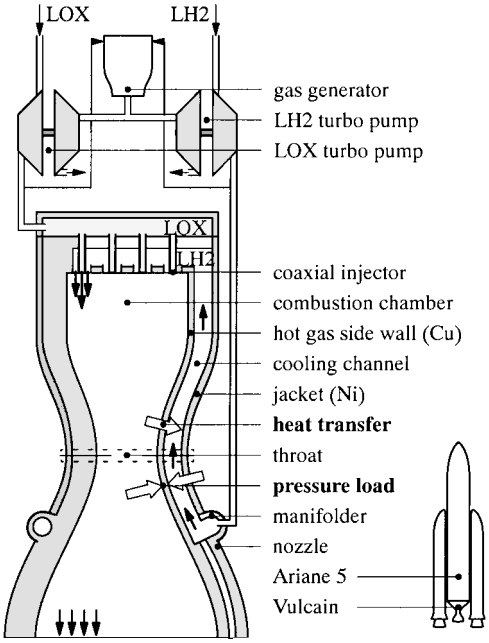


**Fig. 1 Schematic view of the regeneratively cooled combustion chamber Vulcain.**

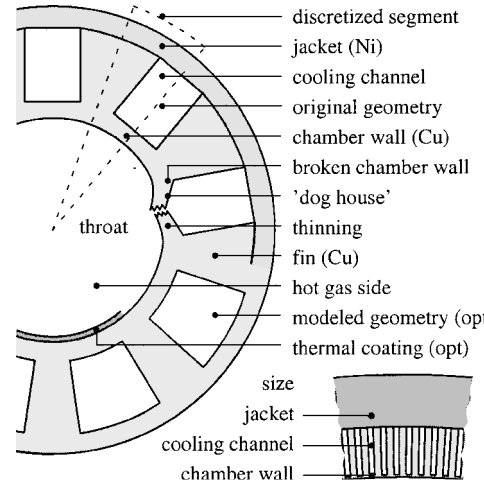


**Fig. 2 Throat of the combustion chamber: modeling, characteristic failure, and optimization model (opt).**

### B. Direct Thermomechanical Problem

The modeling and the simulation of the direct thermomechanical problem is focused on the coolant flow and the deformation of the combustion chamber wall. The effect of the combustion chamber flow and heating on the hot-gas side is introduced due to prescribed boundary conditions, namely, the combustion chamber pressure $p_h$ and the hot-gas-side heat flux $q_h = \alpha_h(\theta - \theta_h)$, obtained from experiments by Fischer et al.[6] The thermomechanical fluid–structure model is subdivided in the coupled fluid flow and thermal field problem and the thermomechanical structural problem, whereby the parts are connected by the heat transfer $q_c = \alpha_c(\theta_c - \theta)$ and the pressure $p_c$ at the shared boundary. For the sake of simplicity, the geometry of the combustion chamber wall and the cooling channel is substituted by a representative geometry, given by a three-dimensional straight cooling channel and thermal structural model and a plane stress thermomechanical structural model as shown in Fig. 3.

### C. Optimization

Based on the direct problem described earlier, the inverse problem can be solved. Within the framework of the inverse problem, loads and material as well as manufacturing restrictions are given, and the design of the combustion chamber should be generated in a way to obtain an optimal behavior with respect to a well-defined objective. The inverse problem is solved by methods of mathematical

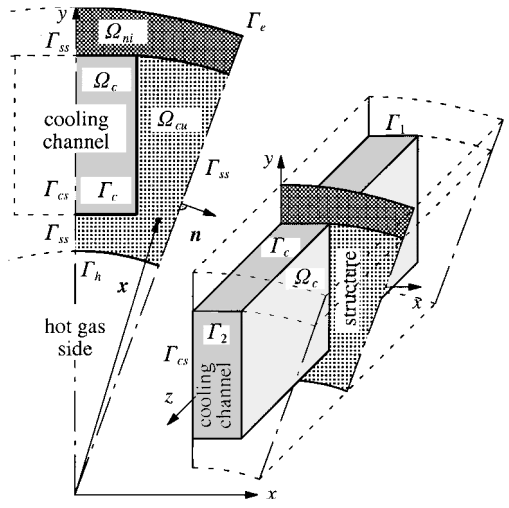


**Fig. 3 Computational model of the combustion chamber.**

programming, where the solution of the direct problem is included to determine the objective and its sensitivity with respect to the design parameters. Practically, the application of optimization methods is restricted to an additional optimization loop in the program code, including, as core, the solution procedure of the direct problem. Consequently, these methods may be applied simply to calculate the optimal design of combustion chambers. Within this paper, the used optimization method and the application to the combustion chamber design are investigated by means of a simplified linear thermomechanical model of the combustion chamber.

## II. Governing Equations

The thermomechanically coupled boundary-value problem of the interacting coolant flow and the combustion chamber's structure is governed by the conservation laws of mass, momentum, and energy, as well as the related boundary conditions, whereby the conservation of mass is explicitly satisfied for the solid domain. Five essential simplifications (assumptions) are made to obtain a system of differential equations that can be solved robustly and effectively by finite element discretization techniques.

1) The system behavior is independent of time; a steady-state formulation is sufficient.

2) The fluid flow is incompressible.

3) The dynamic viscosity $\mu$ and density $\rho$ of the fluid are independent of the temperature.

4) The isotropic conductivities $\Lambda$ of the fluid and the structure are independent of the temperature.

5) The deformations of the structure are small; a geometrically linear description is sufficient.

The computational model of the combustion chamber, the solid and fluid subdomains, and the boundaries for the formulation of the thermomechanical fluid–structure interaction problem are shown in Fig. 3. Based on assumptions 1–5, the thermomechanical system of the combustion chamber is uniquely described by the velocity field of the fluid $\dot{\boldsymbol{u}}$, the coupled temperature field of the fluid and the structure $\theta$, the displacement field of the structure $\boldsymbol{u}$, and the internal variables of the nonlinear material law ($\boldsymbol{\varepsilon}^p$ and $\boldsymbol{\alpha}$).

### A. Mechanical Fluid Field

If assumptions 1–3 are considered, the Navier–Stokes equations, explicitly the conservation of mass and momentum, circumstantiate that the fields of the velocity vector $\dot{\boldsymbol{u}}(\boldsymbol{x}, p)$ and the pressure $p(\boldsymbol{x}, \dot{\boldsymbol{u}})$ are independent of the temperature field $\theta(\boldsymbol{x}, \dot{\boldsymbol{u}}, p)$ (for example, see Hirsch[7]). The conservation of mass is given by the divergence-free velocity field:

$$\nabla \cdot \dot{\boldsymbol{u}} = 0 \quad \forall \quad \boldsymbol{x} \in \Omega_c \tag{1}$$

If no external forces are applied, the equation of motion is given as a function of the density $\rho$, the velocity vector $\dot{\boldsymbol{u}}(\boldsymbol{x})$, and the stress tensor $\boldsymbol{\sigma}(\boldsymbol{x}, \dot{\boldsymbol{u}})$:

$$\nabla \cdot (\rho \dot{\boldsymbol{u}} \otimes \dot{\boldsymbol{u}} - \boldsymbol{\sigma}) = \boldsymbol{0} \quad \forall \quad \boldsymbol{x} \in \Omega_c \tag{2}$$

The stress tensor $\boldsymbol{\sigma}$ is defined by the constitutive law of a Newtonian fluid in terms of the pressure $p(\boldsymbol{x})$, the isotropic dynamic viscosity $\mu$, and the viscous shear tensor $\boldsymbol{\tau}(\boldsymbol{x}, \dot{\boldsymbol{u}})$:

$$\boldsymbol{\tau} = 2\mu \nabla^{\text{sym}} \dot{\boldsymbol{u}} = \mu[\nabla \dot{\boldsymbol{u}} + \nabla^T \dot{\boldsymbol{u}}], \qquad \boldsymbol{\sigma} = -p\boldsymbol{I}_2 + \boldsymbol{\tau} \tag{3}$$

where $\boldsymbol{I}_2$ is the second-order identity tensor. When Eqs. (1) and (3) are considered, the pressure can be determined for a prescribed velocity field by the evolution of the divergence of Eq. (2):

$$\nabla^2 \cdot (\dot{\boldsymbol{u}} \otimes \dot{\boldsymbol{u}} + p\boldsymbol{I}_2) = 0 \tag{4}$$

Dirichlet boundary conditions are given by the velocity at the inlet, the nonslip condition at the cooling channel wall, the symmetry conditions, and the pressure at the outlet:

$$\begin{gathered} \dot{\boldsymbol{u}} \cdot \boldsymbol{n} = \dot{u}_1, \qquad \dot{\boldsymbol{u}} \times \boldsymbol{n} = \boldsymbol{0} \quad \forall \quad \boldsymbol{x} \in \Gamma_1 \\ \dot{\boldsymbol{u}} = \boldsymbol{0} \quad \forall \quad \boldsymbol{x} \in \Gamma_c \\ \dot{\boldsymbol{u}} \cdot \boldsymbol{n} = 0 \quad \forall \quad \boldsymbol{x} \in \Gamma_{cs} \\ p = p_2 \quad \forall \quad \boldsymbol{x} \in \Gamma_2 \end{gathered} \tag{5}$$

### B. Thermal Fluid Field

If no heat sources are applied and assumption 1 is considered, the conservation of energy is given in terms of the specific total energy flux by convection $\rho \dot{\boldsymbol{u}} e_t(\boldsymbol{x}, \dot{\boldsymbol{u}}, \theta)$, the energy flux by diffusion $\boldsymbol{q}(\boldsymbol{x}, \theta)$, and the work performed by the internal stresses $\boldsymbol{\sigma} \cdot \dot{\boldsymbol{u}}$:

$$\nabla \cdot (\rho \dot{\boldsymbol{u}} e_t + \boldsymbol{q} - \boldsymbol{\sigma} \cdot \dot{\boldsymbol{u}}) = 0 \quad \forall \quad \boldsymbol{x} \in \Omega_c \tag{6}$$

where the total energy $e_t = \dot{\boldsymbol{u}}^2/2 + e$ is given by the sum of the kinetic energy $\dot{\boldsymbol{u}}^2(\boldsymbol{x})/2$ and the internal energy $e(\boldsymbol{x}, \theta)$. Furthermore, the constitutive laws connect the temperature field to the heat flux by diffusion and the specific internal energy to the temperature field,

$$\boldsymbol{q} = -\Lambda \nabla \theta, \qquad e = c\theta \tag{7}$$

where $\Lambda$ is the isotropic conductivity and $c$ the specific heat coefficient. Thermal boundary conditions are given at the inlet and outlet, the cooling channel wall, and the symmetry plane $\Gamma_{cs}$:

$$\begin{gathered} \theta = \theta_1 \quad \forall \quad \boldsymbol{x} \in \Gamma_1 \\ \theta = \theta_s \quad \forall \quad \boldsymbol{x} \in \Gamma_c \\ \boldsymbol{q} \cdot \boldsymbol{n} = 0 \quad \forall \quad \boldsymbol{x} \in \{\Gamma_{cs}, \Gamma_2\} \end{gathered} \tag{8}$$

### C. Thermal Structural Field

When a stationary temperature field $\theta(\boldsymbol{x})$ (assumption 1) is assumed, the energy balance law connects the heat flux $\boldsymbol{q}(\boldsymbol{x}, \theta)$ to the internal dissipation $\mathcal{D}_{\text{int}}(\boldsymbol{x}, \boldsymbol{u}, \theta)$ resulting from the plastic deformation (for example, see Zienkiewicz and Taylor[8]):

$$\nabla \cdot \boldsymbol{q} = \mathcal{D}_{\text{int}} \quad \forall \quad \boldsymbol{x} \in \{\Omega_{\text{cu}}, \Omega_{\text{ni}}\} \tag{9}$$

The Fourier law defines the heat flow as function of the temperature gradient,

$$\boldsymbol{q} = -\Lambda \nabla \theta \tag{10}$$

All boundary conditions of the thermal field are Neumann boundary conditions, described by symmetry conditions, adiabatic conditions at the environment surface, the experimentally evaluated film coefficient $\alpha_h$ at the hot-gas side, and the numerically evaluated film coefficient $\alpha_c$ at the coolant side with respect to the bulk temperatures $\theta_h$ and $\theta_c$:

$$\begin{gathered} \boldsymbol{q} \cdot \boldsymbol{n} = 0 \quad \forall \quad \boldsymbol{x} \in \{\Gamma_{ss}, \Gamma_e\} \\ \boldsymbol{q} \cdot \boldsymbol{n} = q_h = \alpha_h(\theta - \theta_h) \quad \forall \quad \boldsymbol{x} \in \Gamma_h \\ \boldsymbol{q} \cdot \boldsymbol{n} = q_c = \alpha_c(\theta - \theta_c) \quad \forall \quad \boldsymbol{x} \in \Gamma_c \end{gathered} \tag{11}$$

### D. Mechanical Structural Field

Considering assumptions 1 and 5, the deformation of the combustion chamber's structure is described by the displacement field $\boldsymbol{u}(\boldsymbol{x}, \theta)$, which is governed by the balance of momentum (for example, see Zienkiewicz and Taylor[8]),

$$\nabla \cdot \boldsymbol{\sigma} = \boldsymbol{0} \quad \forall \quad \boldsymbol{x} \in \{\Omega_{\text{cu}}, \Omega_{\text{ni}}\} \tag{12}$$

where $\boldsymbol{\sigma}(\boldsymbol{x}, \theta, \boldsymbol{\varepsilon}, \boldsymbol{\alpha})$ represents the Cauchy stress tensor given as function of the temperature field, the Green strain tensor $\boldsymbol{\varepsilon}(\boldsymbol{x}, \boldsymbol{u})$, and the internal variables $\boldsymbol{\alpha}(\boldsymbol{x}, \boldsymbol{u}, \theta)$. The stress tensor is related to this field variables by the constitutive law as briefly described in Sec. II.E. In accord with a geometrically linear description (assumption 5), the strain tensor is defined by the symmetric part of the displacement gradient,

$$\boldsymbol{\varepsilon} = \nabla^{\text{sym}} \boldsymbol{u} = \tfrac{1}{2}[\nabla \boldsymbol{u} + \nabla^T \boldsymbol{u}] \tag{13}$$

The associated boundary conditions are the symmetry conditions, the pressure-free environment, the hot-gas-side pressure $p_h$, and the cooling channel pressure $p_c$:

$$\begin{aligned} \boldsymbol{u} \cdot \boldsymbol{n} &= 0 \quad \forall \quad \boldsymbol{x} \in \Gamma_{ss} \\ \boldsymbol{n} \cdot \boldsymbol{\sigma} \cdot \boldsymbol{n} &= 0 \quad \forall \quad \boldsymbol{x} \in \Gamma_{e} \\ \boldsymbol{n} \cdot \boldsymbol{\sigma} \cdot \boldsymbol{n} &= p_h \quad \forall \quad \boldsymbol{x} \in \Gamma_{h} \\ \boldsymbol{n} \cdot \boldsymbol{\sigma} \cdot \boldsymbol{n} &= p_c \quad \forall \quad \boldsymbol{x} \in \Gamma_{c} \end{aligned} \tag{14}$$

### E. Nonlinear Material Law

The solution of the equation of motion (12) requires the calculation of the stress tensor as a function of the total strains, the temperature, and the internal variables. Therefore, a material model has been chosen that can be characterized by the von Mises yield function, associative small strain plasticity, and a linear kinematic hardening rule. The basic theory, for example, described by Hill[9] and Simo and Hughes,[10] will be summarized and applied to the calculation of the rocket combustion chamber.

As a basis for the definition of the nonlinear material behavior, the infinitesimal strain tensor $\boldsymbol{\varepsilon}$ is decomposed in an elastic $\boldsymbol{\varepsilon}^e(\boldsymbol{x}, \boldsymbol{u}, \theta)$, a thermal $\boldsymbol{\varepsilon}^\theta(\boldsymbol{x}, \theta)$, and a plastic part $\boldsymbol{\varepsilon}^p(\boldsymbol{x}, \boldsymbol{u}, \theta)$,

$$\boldsymbol{\varepsilon} = \nabla^{\text{sym}} \boldsymbol{u} = \boldsymbol{\varepsilon}^e + \boldsymbol{\varepsilon}^\theta + \boldsymbol{\varepsilon}^p \tag{15}$$

Thermal strains are determined by the thermal expansion coefficient $\alpha$ and the difference between the current temperature $\theta$ and the reference temperature $\theta_r$, which represents the temperature of manufacturing,

$$\boldsymbol{\varepsilon}^\theta = \alpha(\theta - \theta_r)\boldsymbol{I}_2 \tag{16}$$

The stress tensor is described by the elastic stress strain relation

$$\boldsymbol{\sigma} = \boldsymbol{C} : \boldsymbol{\varepsilon}^e = \boldsymbol{C} : (\boldsymbol{\varepsilon} - \boldsymbol{\varepsilon}^p - \boldsymbol{\varepsilon}^\theta) \tag{17}$$

and the constitutive tensor $\boldsymbol{C}(\theta)$ given in terms of the temperature-dependent Young's modulus $E(\theta)$, the Poisson ratio $\nu$, and the forth-order identity tensor $\boldsymbol{I}_4$,

$$\boldsymbol{C} = \frac{E\nu \boldsymbol{I}_2 \otimes \boldsymbol{I}_2}{(1-2\nu)(1+\nu)} + \frac{E}{1+\nu}\boldsymbol{I}_4 \tag{18}$$

Plastic deformations are characterized by the von Mises yield function with a linear kinematic hardening rule:

$$f(\boldsymbol{\sigma}, \boldsymbol{\alpha}, \theta) = \|\text{dev}\boldsymbol{\sigma} - \boldsymbol{\alpha}\| - \sqrt{\tfrac{2}{3}}\sigma_Y \tag{19}$$

where $\boldsymbol{\alpha}$ is the second-order tensor of internal hardening variables, $\sigma_Y(\theta)$ is the temperature-dependent yield stress, and $\text{dev}\boldsymbol{\sigma}$ is the deviator of the stress tensor. The flow rule and the linear kinematic hardening law for associative plasticity are formulated in evolution equations by means of the consistency parameter $\dot{\gamma}$,

$$\dot{\boldsymbol{\varepsilon}}^p = \frac{\partial \boldsymbol{\varepsilon}^p}{\partial t} = \dot{\gamma}\frac{\text{dev}\boldsymbol{\sigma} - \boldsymbol{\alpha}}{\|\text{dev}\boldsymbol{\sigma} - \boldsymbol{\alpha}\|} = \dot{\gamma}\boldsymbol{m} \tag{20}$$

where $\boldsymbol{m}$ is the normal vector of the yield surface defining the direction of the plastic flow. The evolution of the kinematic hardening variables is defined in terms of the kinematic hardening modulus $H(\theta)$, which is related to $E(\theta)$ and the tangent modulus $T(\theta)$,

$$\dot{\boldsymbol{\alpha}} = \dot{\gamma}\tfrac{2}{3}H\boldsymbol{m} = \dot{\gamma}\tfrac{2}{3}[ET/(E-T)]\boldsymbol{m} \tag{21}$$

Furthermore, the Kuhn–Tucker loading/unloading conditions $\dot{\gamma} \geq 0$, $f \leq 0$, and $\dot{\gamma} f = 0$ and the consistency condition $\dot{\gamma}\dot{f} = 0$ have to be satisfied. For plastic deformations, defined by $\dot{\gamma} > 0$, the consistency condition, the time derivative of the yield function [Eq. (19)], and the consistency parameter can be determined:

$$\dot{\gamma} = 3E/[3E + 2(1+\nu)(H + \sigma_Y)]\boldsymbol{m}:\dot{\boldsymbol{\varepsilon}} \tag{22}$$

Application of Eqs. (17), (20), and (22) yields the relation between the rates of the stress and strain tensors:

$$\dot{\boldsymbol{\sigma}} = \boldsymbol{C} : (\dot{\boldsymbol{\varepsilon}} - \dot{\boldsymbol{\varepsilon}}^p - \dot{\boldsymbol{\varepsilon}}^\theta) = \boldsymbol{C} : (\dot{\boldsymbol{\varepsilon}} - \boldsymbol{m}\dot{\gamma}) = \boldsymbol{C}^{\text{ep}} : \dot{\boldsymbol{\varepsilon}} \tag{23}$$

where the continuum elasto–plastic tangent operator $\boldsymbol{C}^{\text{ep}}$ is identical to $\boldsymbol{C}$ for $\dot{\gamma} = 0$ and calculated by

$$\boldsymbol{C}^{\text{ep}} = \boldsymbol{C} - \frac{3E^2 \boldsymbol{m} \otimes \boldsymbol{m}}{3(1+\nu)E + 2(1+\nu)^2(H + \sigma_Y)} \tag{24}$$

otherwise. Finally, the internal dissipation $\mathcal{D}_{\text{int}}$ is given in terms of the plastic strain work $\boldsymbol{\sigma}:\dot{\boldsymbol{\varepsilon}}^p$ and the work done by the hardening variables $\boldsymbol{\alpha}$ and the derivative of the yield function $\partial f(\boldsymbol{\sigma}, \boldsymbol{\alpha})/\partial \boldsymbol{\alpha}$:

$$\mathcal{D}_{\text{int}} = \boldsymbol{\sigma} : \dot{\boldsymbol{\varepsilon}}^p + \boldsymbol{\alpha} : \frac{\partial f(\boldsymbol{\sigma}, \boldsymbol{\alpha})}{\partial \boldsymbol{\alpha}}\dot{\gamma} = (\boldsymbol{\sigma} - \boldsymbol{\alpha}) : \dot{\boldsymbol{\varepsilon}}^p \tag{25}$$

## III. Solution Technique

The earlier described multiple field boundary-value problem will be simulated by application of the present coupled field solution strategy and the finite element method.

### A. Coupled Field Problem

To summarize the preceding sections, the coolant flow, the heat transfer, and the structural deformation are completely described by differential equations coupled by field variables and boundary values shown in Fig. 4. In the middle of this diagram, the differential equations are shown. The left-hand side demonstrates the coupling of these equations from the top to the bottom, whereas the right-hand side shows the coupling in the opposite direction. As already mentioned, the velocity field of the coolant flow is independent of the other fields but influences the thermal field of the fluid, as well as the displacement field of the structure. In contrast to this, the other fields are fully coupled. However, if a further assumption is introduced, the solution process will be significantly simplified.

6) In comparison to the high thermal loading of the combustion chamber structure across the boundaries, the influence of the internal dissipation $\mathcal{D}_{\text{int}}$ to the thermal field is negligible.

Assumption 6 leads to an only one-way-coupled thermomechanical problem of the structure; see Fig. 4 for $\mathcal{D}_{\text{int}} \approx 0$. Finally, the earlier explained simplifications yield the following sequential solution strategy.

1) Solve the nonlinear system of differential equations (1) and (2) of the fluid for the velocity field $\dot{\boldsymbol{u}}(\boldsymbol{x})$.

2) Solve the coupled energy equations (6) and (9) of the fluid and the solid domain for the temperature field $\theta(\boldsymbol{x}, \dot{\boldsymbol{u}})$.

3) Solve nonlinear balance of momentum (12) of the structure for the displacement field $\boldsymbol{u}(\boldsymbol{x}, \theta)$.

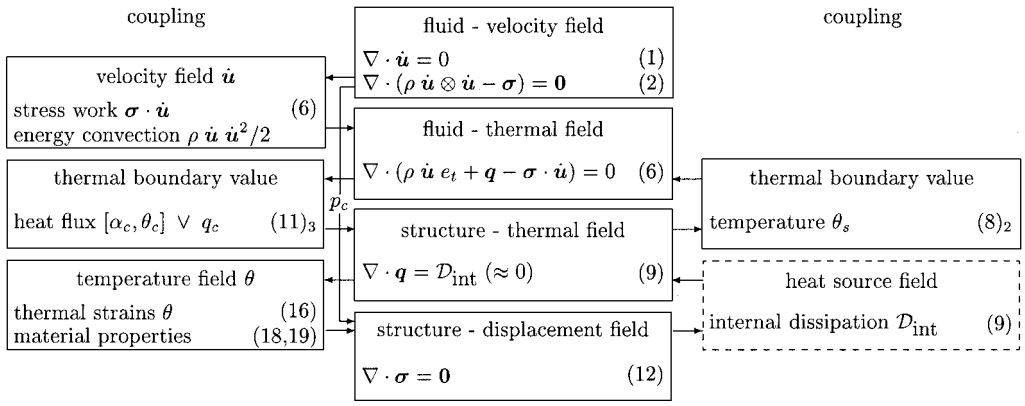


**Fig. 4 Coupling of the thermomechanical fluid–structure problem.**

Note that steps 1 and 3 require only standard discretization and nonlinear solution methods, whereas the execution of step 2 enforces the coupled solution of the thermal fields of the fluid and the structure. This problem results in linear differential equations if the dynamic viscosity $\mu$ and the conductivity $\Lambda$ of the fluid are assumed to be constant within the considered temperature range (assumptions 3 and 4).

The coupling of the thermal fields $\theta(\boldsymbol{x})\ \forall \boldsymbol{x} \in \{\Omega_c, \Omega_{\text{cu}}, \Omega_{\text{ni}}\}$ can be realized based on the equivalence of the energy balance of the fluid and the structure [Eqs. (6) and (9)]. Consequently, the coupled field problem can be solved by a pure fluid code introducing the field condition

$$\dot{\boldsymbol{u}} = \mathbf{0} \quad \forall \quad \boldsymbol{x} \in \{\Omega_{\text{cu}}, \Omega_{\text{ni}}\} \tag{26}$$

as proposed by Emery et al.[11] Based on this statement, the thermal field of the combustion chamber can be calculated in a single calculation. However, with respect to the following finite element solution technique of the structure, first the complete three-dimensional temperature distribution of the combustion chamber is calculated and the heat flux $q_h$ and the temperature $\theta\ \forall \boldsymbol{x} \in \Gamma_c$ at the position of the plane structural analysis are determined by a postprocessing procedure, and second, they are used as thermal boundary condition to the one-way coupled plane thermomechanical structural problem. This step by step strategy is favored because it allows the combined three- and two-dimensional model, as well as different adapted finite element meshes, for the fluid and structural analyses of the combustion chamber, see Fig. 6.

### B. Modeling of Turbulence

Note that Secs. II.A and II.B constitute a complete description of the fluid, which can be solved directly for laminar as well as for turbulent flows. Nevertheless, for the direct solution of turbulent flows, a very fine discretization is required, which is not realizable yet even on super computers for the complete cooling channel flow. To solve this kind of flow with a finite number of elements, the effect of the turbulent motion will be described by the averaging of the turbulent quantities and the additional modeling of turbulence by the $k$–$\varepsilon$ model (Launder and Spalding[12]). Herein, the state variables $\dot{\boldsymbol{u}}$, $p$, and $\theta$ in Eqs. (2), (4), and (6) are averaged quantities, and the dynamic viscosity $\mu$ in Eq. (3) and the conductivity $\Lambda$ in Eq. (7) have to be substituted by the related effective values $\mu_{\text{eff}}$ and $\Lambda_{\text{eff}}$ calculated as the sum of the molecular and turbulent quantities:

$$\mu_{\text{eff}} = \mu + \mu_t, \qquad \Lambda_{\text{eff}} = \Lambda + \Lambda_t \tag{27}$$

The turbulent diffusive transport coefficients $\mu_t$ and $\Lambda_t$ are calculated based on the $k$–$\varepsilon$ model (For details see Woschnak and Kuhl.[13]).

### C. Discretization of the Fluid

The solution algorithm for the fluid flow analysis applies a Galerkin finite element approach to transform the set of partial differential equations into a system of algebraic equations for the primary unknowns. For each degree of freedom, the transport equation can be formulated as a stationary problem. In this analysis, the transport equations consist of an advective and a diffusive term. For the discretization of the advective term, the streamline up-wind approach (for example, Rice and Schnipke[14]) has been used due to stabilization requirements. For the discretization of the diffusion terms, the standard method of the weighted residual (for example, Zienkiewicz and Taylor[8]) is applied.

The solution of the resulting algebraic equation system of the fluid flow uses an uncoupled approach. This means, that each field variable is solved in a sequential way with intermediate values of the other quantities from the previous global iteration. A segregated velocity–pressure solution algorithm, called the fractional step method, is applied (compare Hirsch[7]).

### D. Integration of the Material Law

The numerical solution of material evolution laws for the plastic strain tensor $\boldsymbol{\varepsilon}^p$ and the internal variable tensor $\boldsymbol{\alpha}$ is realized as proposed by Simo and Hughes.[10] Therefore, the initial value of the internal variable tensor has to be defined, and the evolution of the internal variables (20) and (21) within the time is integrated by the implicit backward Euler scheme. The calculation of the stresses, strains, and the elasto–plastic tangent at the end of the time step is realized by an operator split in a purely elastic step and a closest-point projection of the trial state onto the yield surface.

### E. Discretization of the Structure

The solution of the differential equations describing the thermal and the mechanical field of the combustion chamber's structure is realized by the finite element method. Because the mechanical problem is nonlinear, the thermal and mechanical load is applied stepwise, and the iterative Newton–Raphson solution strategy is used in every load step. Because the mentioned methods are familiar to the reader, we only refer to the related literature (for example, Zienkiewicz and Taylor[8] and Crisfield[15]).

## IV. Thermomechanical Analysis of Rocket Engine Vulcain

To demonstrate the performance and efficiency of the proposed solution strategy, it will be applied to the analysis of the currently employed liquid hydrogen/oxygen main engine Vulcain of the European space transport system Ariane V. The geometry of the cooling channel and the structural model are summarized in Fig. 5, (also compare Fig. 3). To avoid the transfer of high-technological knowledge of the producing industry, the given data set represents only a qualitative model of the combustion chamber, published by Fröhlich et al.,[16] Fischer et al.,[6] and Popp and Schmidt.[17] The material properties are summarized in Table 1.

**Table 1 Material properties of hydrogen, copper alloy, and nickel**

| Modeling | | Young's modulus $E$, GPa | Tangent modulus $T$, MPa | Yield stress $\sigma_Y$, MPa | Poisson's ratio $\nu$ | Dynamic viscosity $\mu$, N · s/m$^2$ | Density $\rho$, kg/m$^3$ | Thermal expansion $\alpha$, 1/K | Conductivity $\Lambda$, W/mK | Specific heat $c$, J/kgK |
|---|---|---|---|---|---|---|---|---|---|---|
| Newtonian fluid | Hydrogen | —— | —— | —— | —— | $6.5173 \times 10^{-6}$ | 49.72 | —— | 0.10657 | 15125 |
| von Mises | Copper alloy | 148–0.073 $\theta$/K | 602–0.690 $\theta$/K | 232–0.138 $\theta$/K | 0.3 | —— | (9130) | $1.72 \times 10^{-5}$ | 310 | (373) |
| Saint Venant–Kirchhoff | Nickel | 193 | —— | $\infty$ | 0.3 | —— | (8910) | $1.22 \times 10^{-5}$ | 75 | (444) |

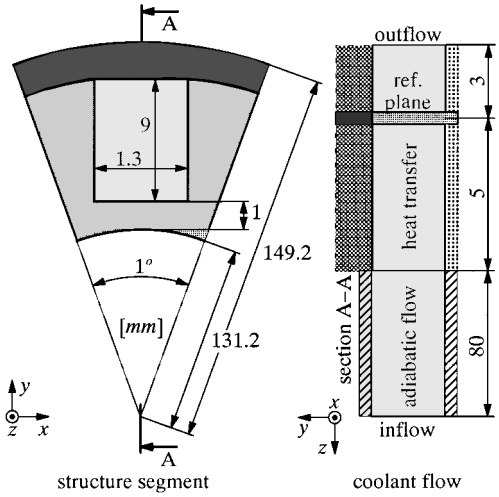


**Fig. 5 Geometry of the combustion chamber model.**

### A. Fluid Flow Simulation

For the analysis of the velocity and temperature fields of the coolant flow, the cooling channel and the structure are discretized by three-dimensional eight-node finite elements (Figs. 5 and 6). In the first part of the cooling channel, an adiabatic flow is assumed, the length, 80 mm, of this part is chosen such that the velocity boundary layer is fully developed. In the second part, the thermal flow between the coolant and the structure is considered. The position of the reference plane, $z = -85$ mm, is chosen such that the thermal boundary layer is not further changed. The flow and boundary conditions are given as follows:

$$\theta_1 = 60\ \text{K}, \qquad u_1 = 160\ \text{m/s}, \qquad p_2 = 14.5\ \text{MPa} \quad (28)$$

For detailed results of the fluid simulation, in particular, for the evolution of the velocity and temperature fields of the coolant, see Woschnak and Kuhl.[13]

### B. Thermal Field and Heat Transfer Analysis

If the boundary conditions at the hot-gas side of the thermal fluid model

$$\alpha_h = 28\ \text{kW/m}^2\ \text{K}, \qquad \theta_h = 3538\ \text{K} \quad (29)$$

are applied, the thermal field of the fluid and structure can be analyzed. Figure 7 shows the resulting circumferential distribution of the local wall temperature $\theta\ \forall \boldsymbol{x} \in \Gamma_c$ and the wall heat flux $q_c\ \forall \boldsymbol{x} \in \Gamma_c$ at the reference plane $z = -85$ mm. The resulting heat transfer by convection, described by the film coefficient $\alpha_c = q_c/(\theta - \theta_c)$ and the bulk temperature $\theta_c = \theta_1$, is later used as a boundary condition for the structural analysis. From earlier results it can be interpreted that the local heat transfer is influenced by the thickness of the boundary layer. The interference of the orthogonal channel walls thickens the boundary layer, and, therefore, a lower thermal gradient coupled with a decrease of the local heat transfer can be observed.

### C. Structural Deformation by Single Loading

For the nonlinear structural analysis, the full pressure and thermal loads are applied in 1000 successive load steps controlled by the load factor $\lambda \in [0, 1]$. Figure 6 shows the discretization of the combustion chamber structure by bilinear plane stress finite elements and the displacement field as the result of fully applied thermal and mechanical loads. The deformed structure clearly shows the shrinking as a result of the decreasing temperature of the nickel jacket. The effect of the high pressure inside the combustion chamber and the thermal strains related to the increase of the temperature of the combustion chamber wall are suppressed by the very stiff jacket. The displacement field confirms this observation. Nevertheless, the largest radial displacements are not on the hot-gas side but in the region of the cooling channel's corner. A detailed analysis of the deformation process is necessary to understand the complex structural response. Therefore, the evolution of the tangential strain components is subdivided in thermal, elastic, and plastic parts [Eq. (15)] and plotted at four characteristic positions as function of the load factor $\lambda \in [0, 1]$ in Fig. 8. Also compare the position of nodes 1–4 and the strain fields $\varepsilon^e_{xx} + \varepsilon^p_{xx}$ in Fig. 9. For all nodes, positive linear thermal strains representing the increasing temperature within the domain $\Omega_{\text{cu}}$ caused by the increase of the load factor are demonstrated. The elastic strains vary linearly until the yield stress is reached. After the beginning of the plastification, small linear changes of the elastic strains related to the temperature-dependent yield stress can be observed. As a result of the global shrinking of the structure, negative tangential plastic strains are generated at the four chosen nodes. A special effect of the combustion chamber's structure can be observed by means of the plastic and total tangential strains of the positions on the hot-gas-side boundary (nodes 1–3). As expected, at nodes 1 and 2, high negative plastic and total strains occur. However, only small negative plastic strain components and positive total strains can be identified at nodes 3 and 4. The reason for this unexpected effect is the high-pressure gradient between the hot-gas side and the cooling channel ($\Delta p = p_c - p_h > 0$) leading to bendinglike deformation of the chamber wall and, consequently, to the reduction of the compressive tangential plastic strains close to this nodes. The evolution of the tangential strains within the successive loading procedure, as presented in Fig. 9 for the small region of the combustion chamber wall, demonstrates clearly the influence of the additional compression effects driven by shrinkage and bending leading to higher compressive strains close to the cooling channel and lower compressive strains in the neighborhood of the hot-gas side. Note that the bending effect is negligible in a linear structural analysis. Only the combination of the high-pressure difference $\Delta p$ and the plastic flow yields the observed significant change of the tangential strain component.

As a result of this structural behavior, the highest plastic strain for single loading is obtained at node 1. If classical lifetime analysis is applied on the basis of a single loading analysis, the failure of the structure occurs at the position of the highest plastic strain. This is in a sharp contrast to experimental observations presented by Quentmeyer[1,2] and Popp and Schmidt,[17] which describe the thinning of the combustion chamber wall, the evolution of a "dog house," and finally the structural failure by a crack in the region of node 3, which is driven by fatigue (compare Fig. 2). Consequently, the analysis of a single loading process is not sufficient to predict the lifetime of combustion chambers. To dissolve the seemingly contradictory results of experimental and numerical investigations, the unloading and the cyclic repetition of the loading/unloading process is studied.

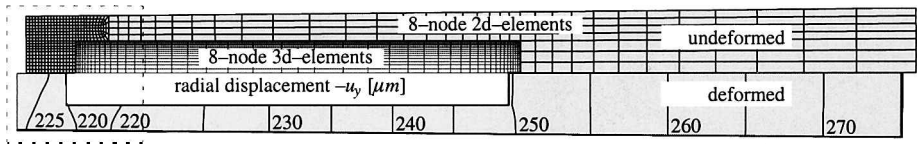


**Fig. 6 Finite element discretization, deformation, and displacement field.**

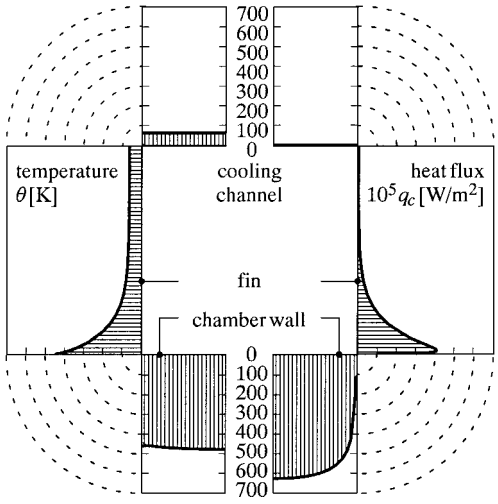


**Fig. 7 Heat transfer at position $z = -85$ mm.**

### D. Structural Deformation by Cyclic Loading

The thermomechanical structural analysis is extended to cyclic loading, where each cycle consists of the loading process similar to the single loading analysis and the unloading process described by a decreasing load factor $\lambda \in [1, 0]$. Because the lifetime of the combustion chamber is primarily restricted by the total value and the range of local plastic strains, the interpretation of the mechanical simulation is focused on the plastic strains. The evolution of the tangential strain component at the four specified nodes during the first unloading process is shown in Fig. 8. Furthermore, the distribution of $\varepsilon^e_{xx} + \varepsilon^p_{xx}$ during the first unloading is plotted in Fig. 9.

The expansion of the global structure during the unloading as consequence of vanishing thermal strains and mechanical boundary conditions leads to elastic unloading and plastic deformation in the opposite direction of the primary plastic deformation. At nodes 3 and 4, the total changes of the plastic strains due to the unloading process are larger compared to the change of the strains related to the loading process. Consequently, the highest tension strain is obtained at the middle of the chamber wall. The cyclic repetition of the loading/unloading process leads to increasing positive plastic strains within every loading cycle. Considering the stress–strain relations given in Fig. 10 (see Fig. 9 for the position of nodes 1–4), the failure mechanism observed by means of experiments can be well understood. The initiation of a crack at node 3 and its propagation to node 4 is associated with the increase of plastic strains in the unloaded state within every load cycle. The increase of $\varepsilon^e_{xx} + \varepsilon^p_{xx}$ at node 2 is smaller compared to the critical nodes. In contrast to this, the evolution of the plastic strain component at node 1 represents nearly a repetition of the first loading cycle. Consequently, the cyclic behavior is stable, and no damage occurs at this node.

### E. Failure Phenomenon

As a consequence of the superposed effects of jacket shrinkage and thermal expansion of the chamber wall, a large plastic tangential compression is obtained at the hot-gas-side wall. Furthermore, the pressure difference $\Delta p$ reduces the constrained deformation and, consequently, the plastic strains in the middle of the chamber wall during the loading process. Nevertheless, the global expansion of

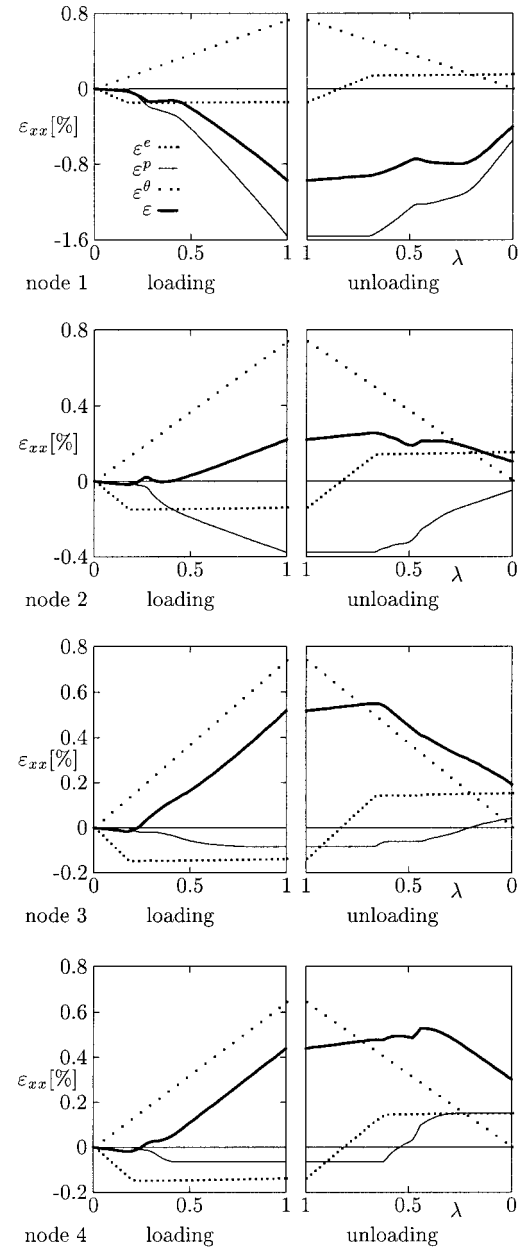


**Fig. 8 Evolution of the elastic, plastic, thermal, and total tangential strain components $\varepsilon_{xx}$ at selected nodes during loading und unloading.**

the structure during the unloading process enforces large tangential strains leading, finally, to an plastic tangential tensile loading. Consequently, the cyclic repetition of this deformation leads to increasing remaining plastic strains within every loading/unloading process (Fig. 10). This causes the thinning of the chamber wall, initiation of microcracks, their propagation, and finally the dog house at the middle of the chamber wall. If the mentioned failure phenomenon is summarized, it can be stated that:

1) the combustion chamber failure is mainly controlled by the temperature difference $\Delta\theta = \theta_h - \theta_e$ of the hot-gas-side wall $\Gamma_h$ and the jacket $\Gamma_e$ and

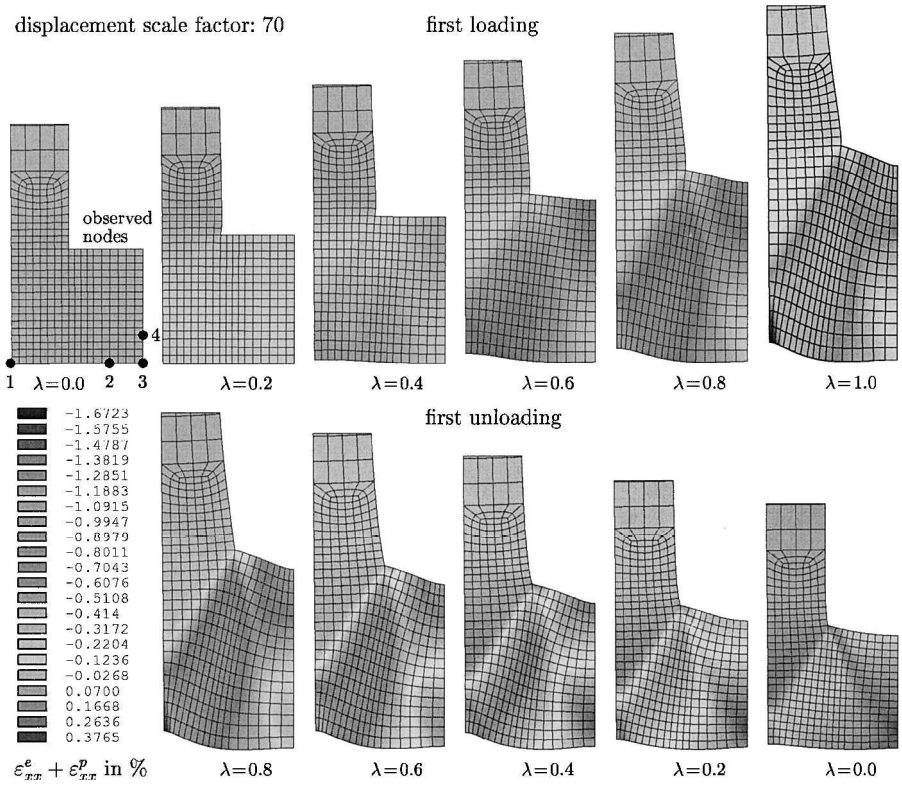


**Fig. 9 Evolution of the tangential strains $\varepsilon^e_{xx} + \varepsilon^p_{xx}$ for the first loading cycle.**

2) the pressure difference $\Delta p = p_c - p_h$ is responsible for the increase of the tensile plastic strains in the crack zone within every load cycle.

### F. Design Improvements

After the main structural failure mechanisms and their controlling parameters are indicated in the preceding section, some system improvements reducing $\Delta\theta$ and $\Delta p$ or avoiding the enforced compressive strains of the combustion chamber wall can be proposed. First, the temperature difference $\Delta\theta$ may be reduced significantly by the following design concepts.

The improvement of the heat transfer between the combustion chamber wall and the coolant will reduce the temperature level of the hot-gas-side wall and, consequently, the thermal and compressive plastic strains. This may by realized by increasing $\alpha_c$ due to a higher surface roughness or additional fins (Fig. 11a), for example. Note that, as consequence of this, a higher pressure loss in the cooling channels, requiring a higher $\Delta p$, will be obtained. As demonstrated by Kazaroff et al.[18] and Jankovsky et al.,[19] the heat transfer can also be improved by using tubular combustion chambers.

$\Delta\theta$ can be decreased by increasing the temperature of the jacket. This may be realized by an external heating of the jacket using combustion products of the gas generator (gas generator cycle). As a disadvantage of this technique, the additional heating of the coolant has to be mentioned. Alternatively, the jacket temperature can be increased by application of a thermal barrier coating on selected surfaces of the cooling channel (Fig. 11b). The thermal isolation of regions with a low heat transfer (compare Fig. 7) yields a heating of the jacket by heat conduction. Because the heat transfer is slightly reduced by this modification, this concept requires additional constructive measures that increase $\alpha_c$.

$\Delta\theta$ can be also decreased by decreasing the temperature $\theta_h$ of the copper alloy. This can be realized due to a mechanically soft thermal barrier coating at the hot-gas side (Fig. 11c). Note that this design concept reduces the heat transfer significantly. Consequently, it is not suitable for the expander cycle.

Second, the negative influence of the pressure difference $\Delta p$ to the cyclic thermomechanical behavior of the combustion chamber may be avoided by the following measures.

Control the cooling channel pressure during the shut down process of the combustion chamber, such that it is adapted to the thermomechanical state of the material, which means that the pressure difference should minimized in this situation.

Reduce the cooling channel pressure in critical regions by an adaption of the cooling channels cross section, which also increases the heat transfer characterized by $\alpha_c$ (Fig. 11f).

Reduce the necessary entrance cooling channel pressure by the use of more manifolders for shorter cooling channels allowing an unchanged injection pressure (Fig. 11g).

Third, the damaging impact of the temperature difference $\Delta\theta$ can be reduced by changing the structural design of the combustion chamber.

If the coupling of the deformations $\boldsymbol{u}$ of the hot-gas-side wall and the nickel jacket is reduced, the compressive plastic strains of the hot-gas-side wall will be decreased. The mechanical decoupling can be realized by the design concept of an elastic liner (Fig. 11d), decoupling inner and outer deformation due to the geometric design, or by the low stiffness compressible material layer between the copper alloy and the nickel jacket (Fig. 11e). The improvement of the lifetime by a design permitting unrestrained thermal expansion of the liner have been earlier investigated by Pavli et al. [20]

## V. Optimization

Previously summarized numerical studies demonstrate that the principle failure phenomenon of combustion chambers can be qualitatively simulated and understood by the interpretation of the numerical results. However, the direct simulation of the thermomechanical deformation process is not suited to lead to an answer of the following typical engineering question: Which design leads to an improved or optimal thermomechanical behavior and, finally, maximizes the lifetime of the structure or optimizes any other property of the combustion chamber? To answer this question, the inverse thermomechanical problem has to be solved. Such kinds of problems are characterized by a given loading and the unknown design, which minimizes a chosen objective function and satisfies simultaneously several constraints. The inverse problem is classically solved by the engineer, who develops the structure, analyzes

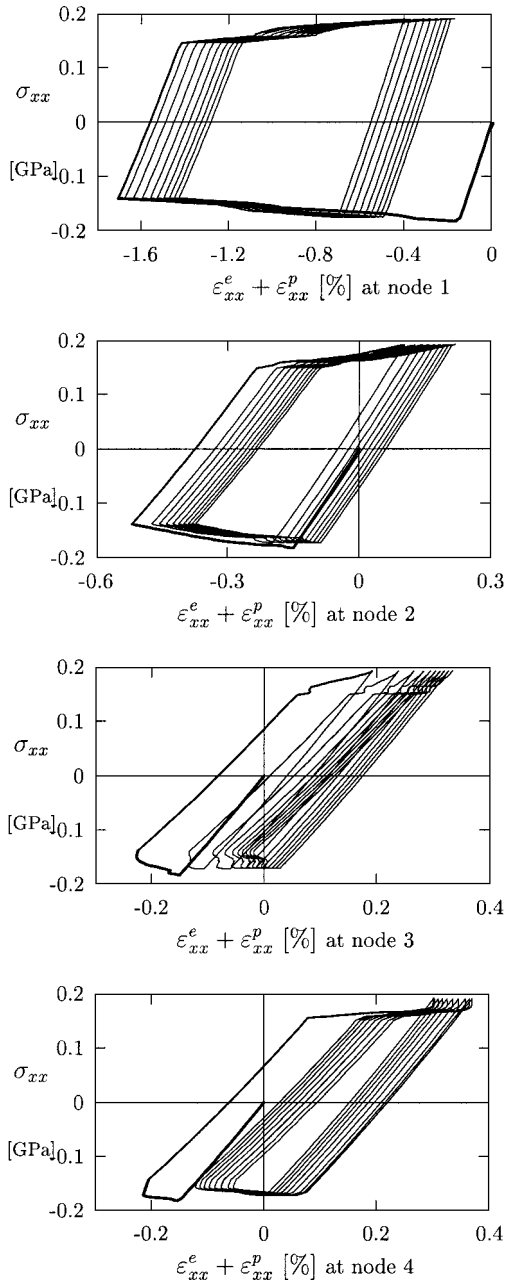


**Fig. 10 Tangential stress–strain relation at selected nodes for cyclic loading.**

the structural behavior, checks constraints, and finally changes the design and repeats the procedure until the structure fulfills all demands and the objective criterion is improved.

A similar procedure is used within the mathematical design optimization process (compare Fig. 12). The initial design of the structure is defined by a set of design variables $\boldsymbol{s}_n = \boldsymbol{s}_0$. The direct solution is applied to check the constraints $\boldsymbol{g}(\boldsymbol{s}_n)$ and to determine the objective function $f(\boldsymbol{s}_n)$, which characterize the quality of the design. In addition to the direct solution, a sensitivity analysis is carried out. Finally, the sensitivity $\nabla_s f(\boldsymbol{s}_n)$ is used within the mathematical programming procedure in which the criterion of the optimal design is checked and the design variables are modified systematically. This mentioned mathematical optimization cycle will be repeated until the optimization criterion $\nabla_s f(\boldsymbol{s}_n) = \boldsymbol{0}$ is satisfied. In contrast to the typical engineering optimization approach, which is based more or less on an educated guess, every design change by mathematical programming does guarantee an improvement of the design, and the optimal construction can be found.

The optimization of the combustion chamber structure is organized as follows: First, the constrained optimization problem is

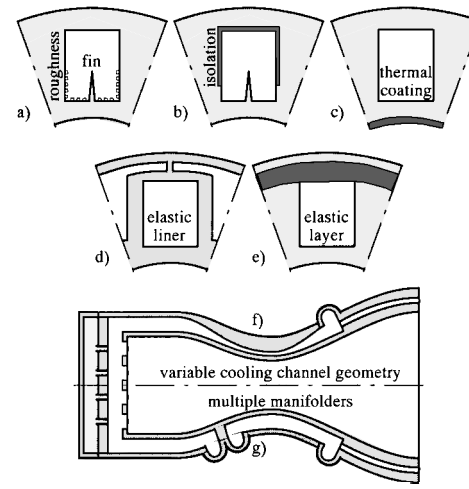


**Fig. 11 Advanced design concepts increasing the lifetime of rocket combustion chambers.**

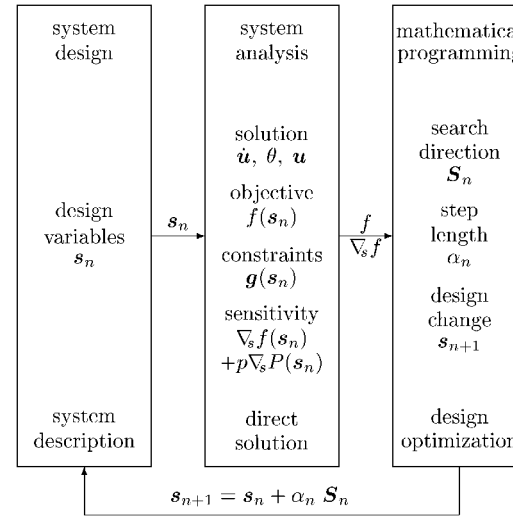


**Fig. 12 Optimization strategy.**

defined, which will, second, be transformed into the unconstrained optimization problem by its penalty formulation, and, finally, solved by mathematical programming methods. For a detailed discussion of optimization methods, refer to Luenberger[21] and Haftka et al.[22]

### A. Constrained Optimization Problem

A constrained optimization problem of the combustion chamber is given by the vector of design parameters $\boldsymbol{s}$ of the combustor and the definition of the objective function

$$f(\boldsymbol{s}) = \min, \qquad \boldsymbol{s} = [s_1, s_2, \ldots, s_k]^T \tag{30}$$

which should be minimized such that simultaneously the constraints

$$\boldsymbol{g}(\boldsymbol{s}) \geq \boldsymbol{0}, \qquad \boldsymbol{g} = [g_1, g_2, \ldots, g_l]^T \tag{31}$$

characterizing the feasible design domain are fulfilled. In general, the objective is an arbitrary scalar-valued function of the design variables $\boldsymbol{s}$ that can be determined through the direct analysis of the combustion chamber discussed in Secs. II–IV. For example, this may be the maximum plastic strain of the structure after one or after a series of direct calculated loading cycles, the predicted lifetime, the temperature difference of the chamber wall and the jacket, the pressure loss in the cooling channel, or the increase of the coolants internal energy due to heat exchange (expander cycle), to point out a few possible objectives. The optimization problem is completed by the definition of the constraints including the restrictions of the design variables $\underline{\boldsymbol{s}}$, $\bar{\boldsymbol{s}}$ characterizing, for example, bounds of manufacturing

or process parameters and $l-2k$ further constraints calculated by the direct analysis of the problem:

$$g_{2i-1}(\boldsymbol{s}) = s_i - \underline{s}_i, \qquad i \in \{1, \ldots, k\}$$
$$g_{2i}(\boldsymbol{s}) = \bar{s}_i - s_i, \qquad i \in \{1, \ldots, k\}$$
$$g_j(\boldsymbol{s}), \qquad j \in \{2k+1, \ldots, l\} \tag{32}$$

where $g_j$ may be the maximum wall temperature defined by the melting temperature of the copper alloy and the minimal cross section of all cooling channels that is necessary for the transport of the fuel with an acceptable pressure loss, respectively.

### B. Unconstrained Optimization Problem

When the exterior penalty function $P(\boldsymbol{s})$ defined by

$$P(\boldsymbol{s}) = \bar{\boldsymbol{g}}(\boldsymbol{s}) \cdot \bar{\boldsymbol{g}}(\boldsymbol{s}), \qquad \bar{g}_i(\boldsymbol{s}) = \max[0, g_i(\boldsymbol{s})] \tag{33}$$

and the penalty factor $p_p$ are introduced, the constrained optimization problem given by Eqs. (30) and (31) can be transformed to an unconstrained one by using the penalty method:

$$Q(\boldsymbol{s}) = f(\boldsymbol{s}) + p_p P(\boldsymbol{s}) = \min \tag{34}$$

The Gâteaux derivative of $Q(\boldsymbol{s})$ with respect to the design variables yields the necessary condition of an optimal design:

$$\frac{\partial Q(\boldsymbol{s})}{\partial \boldsymbol{s}} = \nabla_s Q(\boldsymbol{s}) = \nabla_s f(\boldsymbol{s}) + p \nabla_s P(\boldsymbol{s}) = 0 \tag{35}$$

The sufficient condition for a minimum is that the second derivative of the unconstrained objective function with respect to the design variables $\nabla_s^2 Q(\boldsymbol{s})$ has to be positive definite. However, because Eq. (35) determines only one vanishing tangential of the objective function, $\nabla_s Q(\boldsymbol{s}) = \boldsymbol{0}$ characterizes only a local and not the global optimum of a, in general, nonconvex objective $Q(\boldsymbol{s})$.

### C. Optimization Algorithms

Numerical methods solving the nonlinear optimization problem described by Eq. (34) are based on the solution of the necessary condition of an optimum (35) by the multidimensional Taylor expansion of $\nabla_s Q(\boldsymbol{s})$ about a given design vector $\boldsymbol{s}_n$:

$$\nabla_s Q(\boldsymbol{s}_{n+1}) = \nabla_s Q(\boldsymbol{s}_n) + \nabla_s^2 Q(\boldsymbol{s}_n)(\boldsymbol{s}_{n+1} - \boldsymbol{s}_n) \tag{36}$$

Because the Hessian $\nabla_s^2 Q(\boldsymbol{s}_n)$ is invertible, the improved design vector is calculated by

$$\boldsymbol{s}_{n+1} = \boldsymbol{s}_n - \left[\nabla_s^2 Q(\boldsymbol{s}_n)\right]^{-1} \nabla_s Q(\boldsymbol{s}_n) \tag{37}$$

where $\boldsymbol{s}_{n+1} - \boldsymbol{s}_n$ is the Newton correction. Unfortunately, the Hessian $\nabla_s^2 Q(\boldsymbol{s}_n)$ is, in general, not known. Therefore, the inverse Hessian $[\nabla_s^2 Q(\boldsymbol{s}_n)]^{-1}$ is approximated by $\alpha_n \boldsymbol{B}_n$,

$$\boldsymbol{s}_{n+1} = \boldsymbol{s}_n - \alpha_n \boldsymbol{B}_n \nabla_s Q(\boldsymbol{s}_n) = \boldsymbol{s}_n + \alpha_n \boldsymbol{S}_n \tag{38}$$

where $\boldsymbol{B}_n$ is generated by an evolution equation in every step of the quasi-Newton iteration. Furthermore, the iterative change of the vector of design variables is interpreted as the product of the search direction $\boldsymbol{S}_n = -\boldsymbol{B}_n \nabla_s Q(\boldsymbol{s}_n)$ and the step length $\alpha_n$. The approximated inverse Hessian is calculated by the conjugate direction method by Polak and Ribiére.[23] Furthermore, the iterative solution of the optimization problem requires the knowledge of the sensitivity $\nabla_s Q$ and the step length $\alpha_n$ for every design set $\boldsymbol{s}_n$. These quantities are calculated numerically by the forward difference method and line search procedure (see Luenberger,[21] Haftka et al.,[22] and Kuhl et al.[5]), respectively.

## VI. Optimization of Rocket Engine Vulcain

To demonstrate the idea and the problems concerning the application of mathematical optimization techniques to the design of rocket combustion chambers, the proposed method will be applied to the analysis of the hydrogen/oxygen combustion chamber shown in Fig. 13. To avoid further complexity of the description and calculation, the computational model of the combustion chamber wall presented in the preceding sections will be significantly simplified by the following assumptions:

1) The heat transfer coefficients and the related bulk temperatures describing the hot-gas side and cooling channel heat transfer are given.

2) The heat transfer coefficients are independent of the design parameters and constant on the surfaces $\Gamma_h$ and $\Gamma_c$.

3) The deformations of the material are purely elastic and described by the Saint Venant–Kirchhoff material model ($\sigma_Y \to \infty$).

4) The shape of the cooling channel is slightly modified to simplify the description of the geometry and the meshing procedure. Furthermore, the combustion chamber is constructed by monolythic copper alloy.

Note that this model is not suited to handle the complex behavior of the combustion chamber because the cooling channel heat transfer is crucially influenced by the geometry and the resulting stresses are much higher than the yield stress. Nevertheless, this simple model is used to introduce mathematical programming methods as design tools for rocket combustion chambers and to study the properties of these methods.

Material properties of the copper alloy and the thermal and mechanical boundary conditions are given in Tables 2 and 3. The design variables $\boldsymbol{s}^T = [\beta, \gamma, t, h, r_e, t_c]$ with upper and lower bounds are chosen as summarized in Fig. 13. Because the maximal

**Table 2 Optimization model, input data material properties**

| Parameter | Copper | Ceramic |
|---|---|---|
| Young's modulus $E$, GPa | 148 | 12 |
| Poisson's ratio $\nu$ | 0.3 | 0.3 |
| Thermal expansion $\alpha$, $10^{-5}$/K | 1.72 | 0.2 |
| Conductivity $\lambda$, W/mK | 310 | 2 |
| Temperature $\underline{\theta}$, K | 293 | 293 |

**Table 3 Optimization model, input data boundary conditions**

| Parameter | Hot gas | Coolant |
|---|---|---|
| Film coefficient $\alpha_i$, kW/m$^2$K | 32 | 100 |
| Bulk temperature $\theta_i$, K | 3528 | 50 |
| Pressure $p_i$, MPa | 10 | 14.2 |

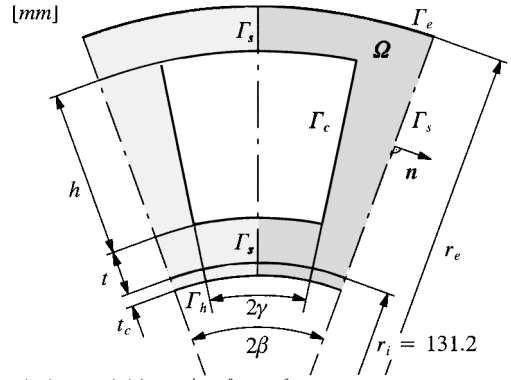


| design variables $\boldsymbol{s}$ | | $\beta[^0]$ | $\gamma[^0]$ | $t$ | $h$ | $r_e$ | $t_c$ |
|---|---|---|---|---|---|---|---|
| standard design | $\boldsymbol{s}_*$ | .5 | .25 | .6 | 5 | 151.2 | 0 |
| lower bound | $\underline{\boldsymbol{s}}$ | .2 | .02 | .1 | 1 | 134.2 | .01 |
| upper bound | $\bar{\boldsymbol{s}}$ | 2 | 1.8 | 2 | 10 | 155.2 | .05 |

**Fig. 13 Optimization model (design set $\boldsymbol{s}_*$).**

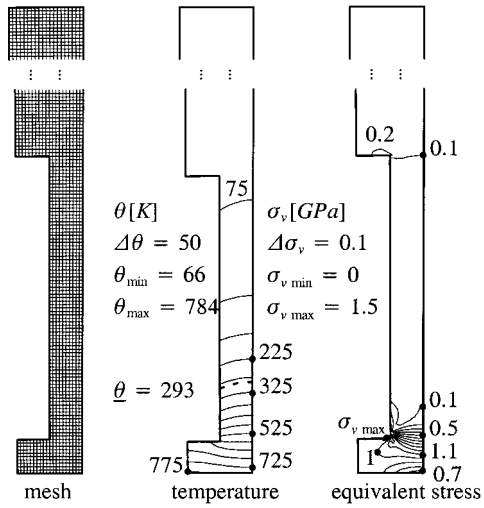


**Fig. 14 Direct solution for design $s_*$.**

scalar-valued equivalent von Mises stress $\sigma_v = \sqrt{\frac{2}{3}}\|\mathrm{dev}\boldsymbol{\sigma}\|$ within the domain $\Omega$ should be optimized, the objective function is given by

$$f(\boldsymbol{s}) = \max_{\Omega} \sigma_v(\boldsymbol{s}) \tag{39}$$

where the local character of the objective $\sigma_v$ is mentioned. As additional constraints, the maximal wall temperature $\bar{\theta} = 1000$ K and the minimal total cross section of all cooling channels given by 80% of the original cross section $A(\boldsymbol{s}_*)$ are introduced:

$$g_{2k+1}(\boldsymbol{s}) = \bar{\theta} - \max_{\Gamma_h} \theta(\boldsymbol{s}), \qquad g_{2k+2}(\boldsymbol{s}) = A(\boldsymbol{s}) - 0.8A(\boldsymbol{s}_*) \tag{40}$$

### A. Characterization of the Objective

Earlier optimization techniques are applied, and the standard design given by the design vector $\boldsymbol{s}_*$ will be analyzed. Furthermore, the character of the chosen objective function and the optimization problem will be studied by means of systematical studies performed by the solution of direct thermomechanical problems using different design sets. Figure 14 demonstrates the discretization by four-node plane stress finite elements and the distribution of the temperature and the equivalent von Mises stress within the structure. As expected after the discussion of the direct problem, the maximal equivalent stress is obtained in the region of the chamber wall. The objective function $f(\boldsymbol{s})$ will be studied by means of the parameter variation $\beta \in [0.2, 2.2]$ and $1-\gamma/\beta \in [0.1, 0.9]$. The contour lines of the objective $f(\boldsymbol{s})$, the temperature constraint $\bar{\theta} - \max_{\Gamma_h} \theta(\boldsymbol{s}) > 0$ for $\bar{\theta} = 1000$ K (fine hatched curve), the geometrical restrictions $\bar{\beta} - \beta > 0$ (coarse hatched horizontal line), $\bar{\gamma} - \gamma > 0$ (vertical hatched line), and the standard design set $\boldsymbol{s}_*$ are plotted in Fig. 15. This representation of the objective characterize the associated optimization problem as follows:

1) The objective function $f(\boldsymbol{s})$ is not convex.

2) One local and the global minimum can be identified within the design space.

### B. Thermal Barrier Coating

The application of the presented optimization strategy to improve the thickness of a thermal barrier coating is shown in Fig. 16. Because this problem is described by only one design parameter $t_c$, the constrained objective function $f(t_c)$, the unconstrained objective function $Q(t_c)$ associated to different penalty factors $p_p$, and the iterative change of the design $t_c$ can be simply visualized. It is obvious that this optimization problem is convex, and consequently, it is easy to find the global optimum, $p_p = 0.01$ and $t_c = 50$ $\mu$m. The good convergence to the optimal design is illustrated by the evolution of the thickness $t_c$ vs the number of iterations $n$.

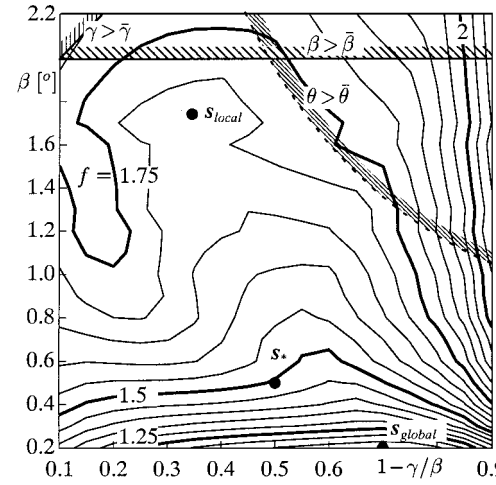


**Fig. 15 Objective function $f(\beta, 1-\gamma/\beta)$ (GPa) and constraints.**

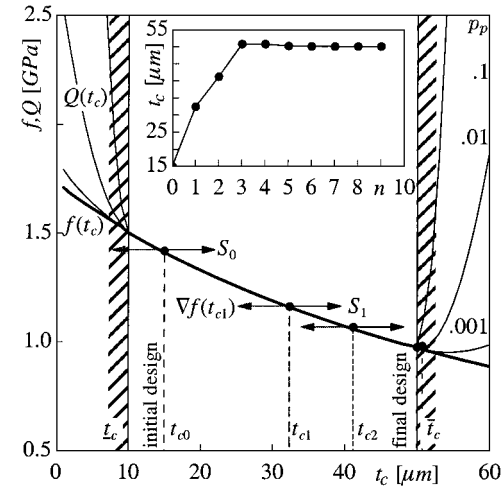


**Fig. 16 Optimization of thermal coating.**

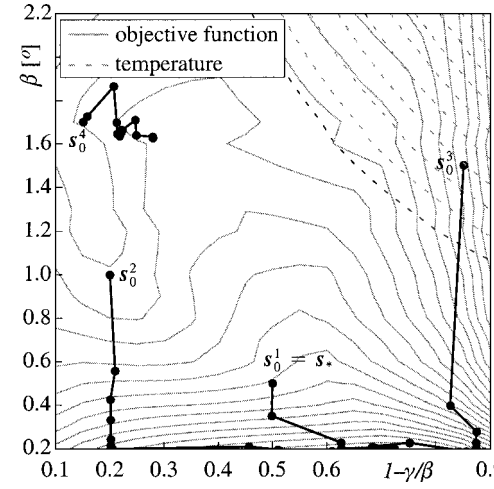


**Fig. 17 Optimization $f(\beta, 1-\gamma/\beta)$ = minimum.**

### C. Two-Dimensional Optimization

The comparison between the parametric study (Sec. VI.A) and optimization methods is demonstrated by means of a two-parameter optimization problem: Minimize $f(\beta, 1-\gamma/\beta)$, such that the constraint $\bar{\theta} > \max_{\Gamma_h} \theta(\boldsymbol{s})$ and the geometrical restrictions are satisfied. The optimization paths for different initial design sets are plotted in Fig. 17. The optimization of the standard design, $\boldsymbol{s}_0^1 = \boldsymbol{s}_*$, leads directly to the solution of the inverse problem given by the global

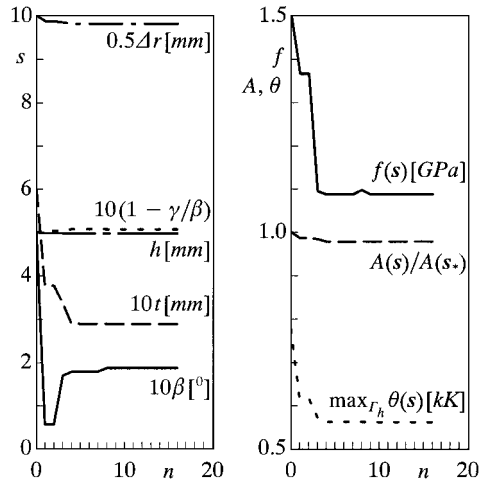


**Fig. 18 Design variables, objective, and constraints.**

optimum. On the other hand, the optimization paths 2 and 3, $s_0^2$ and $s_0^3$, strictly reduce the parameter $\beta$ until the related penalty term is activated. Then, the search direction changes significantly, and finally, the global optimum is obtained. Because one local optimum, $s_{\text{local}}$, is expected on the basis of the parametric study documented in Fig. 15, initial design sets near this minimum have been tested. In one of these tests, the optimization of initial design $s_0^4$ results in a local optimum far away from the global optimum. In general, the investigated studies allow the statement that optimization methods are able to improve an initial design significantly but do not guarantee that the global minimum can be found for every initial design set.

### D. Chamber Wall Design

The simultaneous optimization of the design parameters $s^T = [\beta, \gamma, t, h, r_e]$ comprises the inverse problem: Minimize $f(s)$, such that the constrains $\bar{\theta} > \max_{\Gamma_h} \theta(s)$ and $A(s) > 0.8\ A(s_*)$ are satisfied. The application of the present optimization method results in the evolution of the design variables, the objective function, and the constraints during the iterative solution process, as shown in Fig. 18. Note that the maximal equivalent von Mises stress and the maximal wall temperature of the optimal design are significantly reduced compared to the initial design, where the total cross section of the cooling channels is approximately constant. As expected, the evolution of the design variables recommend the increase of the number of cooling channels (decrease $\beta$) and the decrease of the chamber wall thickness $t$ to improve the combustion chamber design.

## VII. Conclusions

A solution strategy of the coupled thermomechanical fluid–structure interaction boundary-value problem of rocket combustion chambers has been developed. Within the framework of the presented method, the discretization and solution of the fluid and solid equations were realized by nonlinear finite element methods. The application to the combustion chamber Vulcain demonstrated the ability of the presented strategy to compute the cooling channel flow, the heat transfer phenomenon, and the deformation process of the structure. Finally, the failure mechanism of the combustion chamber during cyclic thermal and mechanical loading was discussed, and improved design concepts were proposed.

In addition to the solution strategy of the direct problem, a design concept for the geometry of a rocket combustion chamber wall, based on mathematical programming techniques, has been suggested and investigated. The practicability of the optimization strategy has been demonstrated in the context of the sizing of a combustion chamber cooling channel. However, it has also been pointed out that the final design may strongly depend on the chosen initial design and being only a local minimum. In summary, optimization methods are well suited for the improvement of a good initial rocked engine design, but are not able to substitute the engineer's education and knowledge, which are essential to interpret the numerical results and to generate a appropriate initial design, respectively.

## Acknowledgment

The presented study is supported by grant from the Bundesministerium für Forschung und Technologie within the research project Nationales Technologieprogramm kryogene Raketenantriebe. This support is gratefully acknowledged.

## References

[1]Quentmeyer, R. J., "Experimental Fatigue Life Investigation of Cylindrical Thrust Chambers," AIAA Paper 77-893, 1977.

[2]Quentmeyer, R. J., "Rocket Combustion Chamber Life-Enhancing Design Concepts," AIAA Paper 90-2116, 1990.

[3]Kuhl, D., Woschnak, A., and Haidn, O. J., "Coupled Heat Transfer and Stress Analysis of Rocket Combustion Chambers," AIAA Paper 98-3373, 1998.

[4]Kuhl, D., "Thermomechanical Analysis of Rocket Combustion Chambers," *Proceedings of the Fourth World Congress on Computational Mechanics*, 1998.

[5]Kuhl, D., Haidn, O. J., Josien, N., and Coutellier, D., "Structural Optimization of Rocket Engine Cooling Channels," AIAA Paper 98-3372, 1998.

[6]Fischer, S. C., Popp, M., and Quentmeyer, R. J., "Thrust Chamber Cooling and Heat Transfer," *Proceedings of the Second International Symposium on Liquid Rocket Propulsion*, 1995.

[7]Hirsch, C., *Numerical Computation of Internal and External Flows*, Vols. 1 and 2, Wiley, New York, 1988.

[8]Zienkiewicz, O. J., and Taylor, R. L., *The Finite Element Method*, Vols. 1–3, Butterworth–Heinemann, Oxford, England, U.K., 2000.

[9]Hill, R., *The Mathematical Theory of Plasticity*, Clarendon, Oxford, England, U.K., 1950.

[10]Simo, J. C., and Hughes, T. J. R., *Computational Inelasticity*, Springer-Verlag, New York, 1998.

[11]Emery, A. F., Cochran, R. J., and Pepper, D. W., "Current Trends in Heat Transfer Computations," *Journal of Thermophysics and Heat Transfer*, Vol. 7, 1993, pp. 193–212.

[12]Launder, B. E., and Spalding, D. B., "The Numerical Computations of Turbulent Flows," *Computer Methods in Applied Mechanics and Engineering*, Vol. 3, 1974, pp. 269–289.

[13]Woschnak, A., and Kuhl, D., "Simulation of Heat Transfer in Regeneratively Cooled Rocket Combustion Chambers," *Proceedings of the European Congress on Computational Methods in Applied Science and Engineering, Computational Fluid Dynamics Conference*, 1998.

[14]Rice, J. G., and Schnipke, R. J., "A Monotone Streamline Upwind Finite Element Method for Convection-Dominated Flows," *Computer Methods in Applied Mechanics and Engineering*, Vol. 48, 1985, pp. 313–327.

[15]Crisfield, M. A., *Non-Linear Finite Element Analysis of Solids and Structures*, Vol. 1, Wiley, Chicester, England, U.K., 1991.

[16]Fröhlich, A., Popp, M., Schmidt, G., and Thelemann, D., "Heat Transfer Characteristics of $H_2/O_2$-Combustion Chambers," AIAA Paper 93-1826, 1993.

[17]Popp, M., and Schmidt, G., "Advanced Cryogenic Thrust Chambers," *Proceedings of the 5th International Symposium, Propulsion in Space Transportation*, 1996.

[18]Kazaroff, J. M., Jankovsky, R. S., and Pavli, A. J., "Hot Fire Test Results of Subscale Tubular Combustion Chambers," NASA TP 3222, 1992.

[19]Jankovsky, R. S., Arya, V. K., Kazaroff, J. M., and Halford, G. R., "Structurally Compliant Rocket Engine Combustion Chamber: Experimental and Analytical Validation," NASA TP 3431, 1994.

[20]Pavli, A. J., Kazaroff, J. M., and Jankovsky, R. S., "Hot Fire Fatigue Testing Results for the Compliant Combustion Chamber," NASA TP 3223, 1992.

[21]Luenberger, D. G., *Introduction to Linear and Nonlinear Programming*, Addison–Wesley, New York, 1984.

[22]Haftka, R. T., Gürdal, Z., and Kamat, M. P., *Elements of Structural Optimization*, Kluwer Academic, Dordrecht, The Netherlands, 1993.

[23]Polak, E., and Ribiére, G., "Note sur la Convergence de Méthodes de Direction Conjuguées," *Revue Francaise d'Informatique Recherche Opertionelle, Serie Rouge*, Vol. 16, 1969, pp. 35–43.